



Experimental and thermodynamic investigations on the chlorine-induced corrosion of HVOF thermal sprayed NiAl coatings and 304 stainless steels at 700 °C



Mingwen Bai, Liam Reddy, Tanvir Hussain*

Faculty of Engineering, University of Nottingham, NG7 2RD, UK

ARTICLE INFO

Keywords:

Nickel aluminide
Stainless steel
HVOF
Biomass
Chlorine
Thermodynamic

ABSTRACT

Alumina-forming β -NiAl coatings were deposited by high velocity oxy-fuel (HVOF) thermal spraying onto 304 stainless steels for protection against chlorine induced corrosion in a biomass-fired boiler. The corrosion test was conducted in a synthetic gas containing 500 ppm HCl with 10 wt% KCl ash deposit at 700 °C for 250 h. Severe corrosion was observed with the fast growing alumina at the coating/substrate interface initiating from sample edges. Possible corrosion mechanism was proposed: as supplied by HCl/KCl, the formation of volatile chlorine/chloride acted as a catalyst and promoted the growth of alumina at relatively lower application temperatures (< 900 °C).

1. Introduction

Biomass fuel is a direct replacement for coal to be utilized in traditional coal-fired power plants without requiring plant operators to invest in expensive combustion modifications and limited modifications to handling, and storage facilities. Nevertheless, biomass fuel, such as recycled wood, straw and agricultural crops, also faces new challenges as it normally contains a high content of alkali metals, chlorine and other corrosive elements [1,2]. It would cause severe high temperature corrosion of metallic heat exchanger surfaces, and leads to material damage, and shortened lifetime [3]. In addition, a surging demand for higher energy efficiency and lower CO₂ emissions has stimulated the rapid development of ultra-supercritical (USC) power plants, where the temperatures will be in excess of 650 °C (e.g. the European AD700 program, the American A-USC (760 °C), and the Japanese A-USC, etc.) [4]. This increasingly harsh environment, however, limits the selection of materials to high-alloy steels and nickel-based alloys that could provide sufficient creep and fireside corrosion resistance [5]. Overlay corrosion-resistant coatings could also be applied to further improve the protection against the aggressive fireside corrosion. High-velocity oxy-fuel (HVOF) thermal spraying is one of the most widely used coating techniques for the deposition of Cr₂O₃-forming and Al₂O₃-forming alloys for high temperature corrosion/oxidation protection [6–8]. Cr₂O₃-forming alloys (e.g. Fe–Cr and Ni–Cr alloys) are most widely sprayed as coatings for corrosion protection [9–14]. However, previous researches have shown that the corrosive alkali chlorides (e.g. KCl) reacts with Cr₂O₃ in the protective scale to form K₂CrO₄ [15–18].

Chlorine could penetrate the oxide scale, forming volatile metal chlorides at the scale metal interface. The breakdown of the Cr₂O₃ scale accelerates corrosion attack by subsequently converting to oxides and releasing the chlorine back to the metal surface [19,20]. Al₂O₃-forming alloys (e.g. Fe–Al, Ni–Al alloys) has provided a viable alternative as coatings for high temperature corrosion protection, although the temperature lower than 700 °C may not be high enough to obtain a protective scale [21,22]. It has been reported that the addition of Al to Fe–Cr alloys is beneficial for the corrosion resistance at 650 °C with KCl salt [23]. An alumina scale formed by pre-oxidation of a FeCrAl alloy at 700 °C for 24 h also showed improvement in resistance against attack by KCl at 600 °C [24]. It was also demonstrated that the reaction of KCl with Al₂O₃ to produce potassium aluminate (KAlO₂) is thermodynamically less favored than K₂CrO₄ at the relevant temperature [25]. In addition, Li et al. [26] investigated the hot corrosion behaviour of various Fe–Cr, Fe–Al and Ni–Al model alloys in air with NaCl–KCl deposit at 670 °C for 48 h. In their study, it was found that, among the three model alloys, the NiAl alloys performed the best corrosion resistance with the greatest inertness to chloride salt and the least attack in chlorine-containing environments. The inter-metallic β -NiAl phase coating has been widely used since the 1960s [27] for the protection of gas turbines blades at high temperatures up to 1000 °C.

In the study, NiAl coatings were deposited by HVOF thermal spray onto 304 stainless steels and then subjected to a corrosion test at 700 °C for 250 h with ash deposit containing 10 wt.% of KCl salt in a synthetic gas containing 5 vol.% O₂, 500 ppm HCl and balance N₂. It is worth noting that other gases, such as H₂O, NO_x and SO_x, etc. were deliberately omitted

* Corresponding author.

E-mail address: tanvir.hussain@nottingham.ac.uk (T. Hussain).

from the synthetic flue gas in order to create a simplified environment. The main focus is to study the sole effect of KCl/HCl on the corrosion behaviour of NiAl coatings and stainless steels substrates for the application of next generation ultra-supercritical biomass-fired boilers. The corrosion products were investigated by scanning electron microscopy (SEM), energy dispersive X-ray (EDX) and X-ray diffraction (XRD) analysis, in comparison with the normal oxidation products in air without KCl and HCl. With the intent of providing further insight into the complex corrosion mechanism that involve both O₂ and Cl₂, and the subsequent formation of the oxides and volatile chlorides, a commercially available software, Thermo-Calc[®], was used to study the equilibrium oxide phases existing in the NiAl + O₂ + Cl₂ system at 700 °C. In the end, a possible corrosion mechanism was proposed based on the thermodynamic calculations with a focus on the O₂ and Cl₂ partial pressures.

2. Experimental

2.1. Powder and substrate

A commercial NiAl powder for thermal spraying (AMPERIT291, fused/crushed, H.C.Starck, UK) was used as feedstock with a nominal composition of Ni69Al31 wt.% and a particle size distribution of 5–45 µm. The NiAl powder was sprayed onto AISI 304 stainless steels substrates (nominal composition Fe-19.0Cr- 9.3 Ni- 2.0Mn- 0.05C wt.%) with a dimension of 60 × 25 × 2 mm.

2.2. HVOF thermal spray process

Substrates were grit blasted with brown alumina (F22, 0.8–1.0 mm) under 6 bar pressure, and cleaned by an ultrasonic acetone bath to remove any embedded alumina particles. The substrates were mounted onto a carousel rotating at 73 rpm with a vertical axis of rotation. Metjet IV, a liquid fuel based HVOF thermal spray system (Metallisation Ltd., UK), was used for thermal spraying of the NiAl coatings with kerosene as the fuel. The coatings were deposited with 16 passes and a powder feed rate of ~30 g/min, resulting in a thickness of ~50 µm (deposition efficiency was limited by the low flowability of the feedstock NiAl powders), and the samples were air-cooled during spraying. The length of the nozzle of the HVOF thermal spray gun was 100 mm and a stand-off distance of 356 mm was used during the spray runs. The flow rates of kerosene and oxygen were 415 mL/min and 800 L/min, respectively; nitrogen was used a carrier gas for the powder. The dimensions of the samples for the corrosion tests were 10 mm × 10 mm, same with our previous studies [28,29]. It is worth noting that since the samples were not fully coated with NiAl coatings, the sample edges may act as an initiation for the corrosion attack.

2.3. Chlorine-induced corrosion test

The experimental setup was designed based on industrial benchmark tests for biomass-fired boiler materials (See Fig. 1). The setup contained a horizontal tube furnace with a stainless steel vessel and the inside of the chamber was entirely lined with high purity alumina. A mass flow controller was used to flow 35 cm³/min of synthetic gas (500 ppm HCl, 5% O₂ and balance N₂) through the chamber during the high temperature corrosion test. This is a simplified flue gas composition in biomass-fired boilers (e.g. forest residue, waste wood, straw), where HCl is formed from burning high Cl containing biomass fuel [30]. KCl salt deposit was prepared by mixing 10 wt.% of KCl (99.9%, VWR Chemicals, UK) and 90 wt.% of Kaolinite (Al₂O₃·2SiO₂·2H₂O, Sigma-Aldrich, UK), a synthetic ash, in an ethanol suspension and applied on the samples surface. The samples were dried before the test and then placed in individual alumina crucibles and exposed to the controlled corrosion environment for 250 h at 700 °C with a KCl deposit flux of ~30 mg/cm². In order to better reveal the chlorine-induced corrosion effect caused by KCl/HCl, a control group (oxidation) was applied,

which were treated in the same horizontal tube furnace at 700 °C for 250 h in air. IMS (Industrial Methylated Spirits, ≥99%) was used to carefully clean the entire tube before and after every test to avoid any contamination. This treatment only involved reactions with O₂ and thus is labelled as oxidation test as a contrast to the corrosion test with KCl/HCl. After the corrosion test, sample surface was cleaned by high pressure air dust blower to remove the residual ash.

2.4. Material characterisation

A scanning electron microscope (SEM, FEI Quanta 650, UK) operated at 20 kV and equipped with an energy dispersive X-ray (EDX) detector (Silicon drift detector size: 150 mm², Oxford Instruments, UK) was used to examine the microstructure and compositions of the feedstock powder and the coating surface and cross-sections under secondary electron (SE) and back-scattered electron (BSE) modes. An X-ray diffractometer (XRD, D500 S Germany) with Cu K α radiation (1.5406 Å) was used to identify the phases present in the powders and coatings in the 20° ≤ 2 θ ≤ 90° range with a step size of 0.05° and dwell time of 2 s. AztecEnergy EDX analysis software (Oxford Instruments, UK) was used to acquire montages images along the entire coatings including both the left and right edges. For the microstructural analysis, the coatings samples were mounted in cold-mounting resin filled with Ballotini glass beads for low shrinkage, and the cross-sections were polished down to a 1 µm finish using a non-aqueous medium.

2.5. Thermo-Calc[®] calculation

Thermodynamic calculation of corrosion products as a function of effective partial pressures of O₂ and Cl₂ at 700 °C was carried out using the commercially available Thermo-Calc[®] software (Version 2016b) following the CALPHAD technique. CALPHAD is originally an abbreviation for CALculation of PHase Diagrams, but was later expanded to refer to Computer Coupling of Phase Diagrams and Thermochemistry. The CALPHAD approach is semi-empirical method based on the sequential modelling of the thermodynamic properties of multicomponent systems, which needs basic amount of experimental data for creation of robust, consistent and reliable set of thermodynamic parameters describing simple systems. Such data allows extrapolation of phase diagrams and thermodynamic properties modelling to regions not studied experimentally and/or to more complex systems [31]. The detailed and very comprehensive description of the CALPHAD method was published by Saunders and Miodownik [32] and by Lukas et al. [33]. An extensive description of the modelling background for Thermo-Calc[®] can be found in reference [34]. Commercial databases: TCS Ni-based Superalloys (TCNi8), TCS Steels/Fe-Alloys (TCFe7), and SGTE Substances (SSUB4) were used for the equilibrium computations [35]. Thermodynamic analysis provides equilibrium phase diagrams aiming at the prediction of corrosion and oxidation products of alloys at high temperatures [36]. It concerns not only compositions, but also O₂ and Cl₂ partial pressures, phase, and temperatures, etc. Thermo-Calc[®] calculation is a useful tool to study the selective oxidation behaviour of alloys, especially those complex multicomponent alloys [37]. The application of Thermo-Calc[®] to provide insight into the alumina-forming and chromia-forming alloys systems has been validated by our previous work [28] and others [38–45].

All calculations were based on fixed concentrations, pressures and temperatures, so as to match the isothermal corrosion test used in the present study. The effective partial pressures p_{O_2} and p_{Cl_2} are considered as a variable and represented by chemical activity (a , the unit is 1) ranging from 1×10^{-60} to 1 atm. The M-Cl₂-O₂ (M = Ni, Al, Fe, and Cr) phase diagrams at 700 °C were calculated by Thermo-Calc[®] using SSUB4 database. The results were validated by comparing with the results calculated by HSC chemistry 6.0 [46]. The input of the conditional parameters are listed in Table 1, which are used for the calculation of the phase composition of the oxides formed on the alloys upon

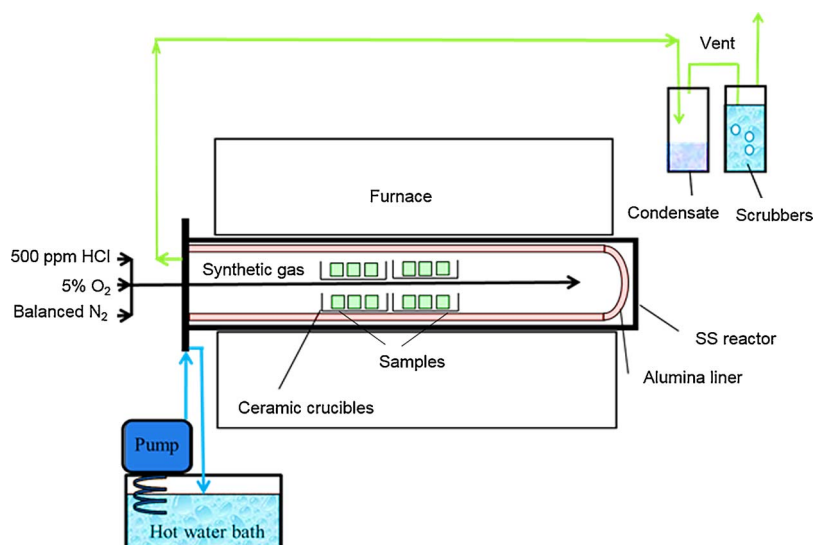


Fig. 1. Schematic diagram of the controlled-atmosphere high temperature corrosion rig.

Table 1
Initialization parameters for Thermo-Calc[®] calculations.

Temperature (°C)	700		
Pressure (atm)	1.0		
System size (mol)	1.0		
Composition (%)	304 Stainless Steel (wt.%)	Fe	Balance
		Cr	19
		Ni	9.3
		Mn	2.0
	β -NiAl (at.%)	Ni	Balance
		Al	40
	γ' -Ni ₃ Al (at.%)	Ni	Balance
		Al	25
Activity of O ₂ (unit is 1)	Min.	1.0×10^{-60}	
	Max.	1.0	
	No. of steps	50	
Activity of Cl ₂ (unit is 1)	Min.	1.0×10^{-60}	
	Max.	1.0	
	No. of steps	50	

equilibrium. Ideally, the composition of β -NiAl and γ' -Ni₃Al phase should be Ni50Al and Ni25Al in mol.% according to the stoichiometric ratio however errors appeared in software when the composition of β -NiAl increased to higher than Ni40Al, at which composition contained 7.14 mol% of γ' phase and 92.86 mol% of β phase. This is a drawback of conducting the Thermo-Calc[®] calculations and the reason remains to be unknown. Nevertheless, according to the calculation results in Fig. 10, the Al content in Ni40Al is sufficient for the formation of exclusive Al₂O₃ with the presence of 0.1 atm O₂ at 700C, which could rule out the adverse effect on the oxidation and corrosion of Ni40Al alloys caused by the impurity of γ' phase.

3. Results

3.1. Feedstock powders

Fig. 2 shows the surface morphology and cross-sections of the NiAl powders under SE mode. The feedstock NiAl powders that were used for HVOF thermal spraying exhibited irregular shapes with angular/polyhedral and rough surfaces. The inset figure shows a particle under BSE mode with no internal porosity and no contrast indicating homogenous composition. Crack can also be seen on the cross-section of powders indicating the brittleness of the intermetallic NiAl phase.

3.2. Phase analysis

Fig. 3 shows the phase analysis of the feedstock powder, the as-sprayed NiAl coatings before and after oxidation and corrosion test. The feedstock has mainly β -phase with a minor impurity of Ni₂Al₃ phase. After spraying, the as-received NiAl coatings retained the β -phase of the NiAl powders with a minor fraction of γ' -Ni₃Al phase. For the oxidation test, no significant phase change in the NiAl coatings is observed, apart from a minor fraction of NiO formed on the coating surface. For the corrosion test, both α -Al₂O₃ and γ' -Ni₃Al phase are identified but only with a minor fraction (the presence of SiO₂ is originated from the kaolinite deposit). In addition, after both heat treatments, the width of XRD peaks decreased, which indicates the relaxation of deformation in coatings.

3.3. Microstructure and composition

Fig. 4 shows the representative cross-sectional microstructure and EDX elemental mappings of the as-sprayed NiAl coating and after both heat treatments under BSE mode. The as-sprayed NiAl coating has an average coatings thickness of 40–50 μ m with a dense and lamellar microstructure. The as-sprayed NiAl coating has an inhomogeneous composition as indicated by the high contrast from the BSE images (See the images in the second row with a higher magnification). It consists of a Ni-rich region (bright area with an approximate composition of 90% Ni + 10%Al) and a Ni-lean region (dark area 67%Ni + 33%Al) as measured by EDX point analysis (See Table 2). After both tests, the Ni-rich regions disappeared and the coatings became uniform with a slight decrease of Al content due to the formation of Al₂O₃ (the black area in the BSE image). The Al₂O₃ content is much higher after corrosion test: (1) on the coating surface; (2) inside the coating lamellar layers; and (3) at the coating/substrate interface. Among the three areas, the most prominent feature is the formation of a coherent and thick Al₂O₃ layer (3 ~ 5 μ m) at the coating-substrate interface.

This feature has been further examined in a wider range of coating length as shown in the montage images along the coating at both the left and right edges, in combination with the EDX mappings (See Fig. 5). It is clearly observed that both the sample edges were severely corroded with the formation of thick Al₂O₃ throughout the coatings but mainly at the coating/substrate interface. More importantly, the corrosion became less aggressive gradually moving from the edges towards the centre of the samples. This full-scale observation from the both edges to the centre of the coatings contributed to a better understanding

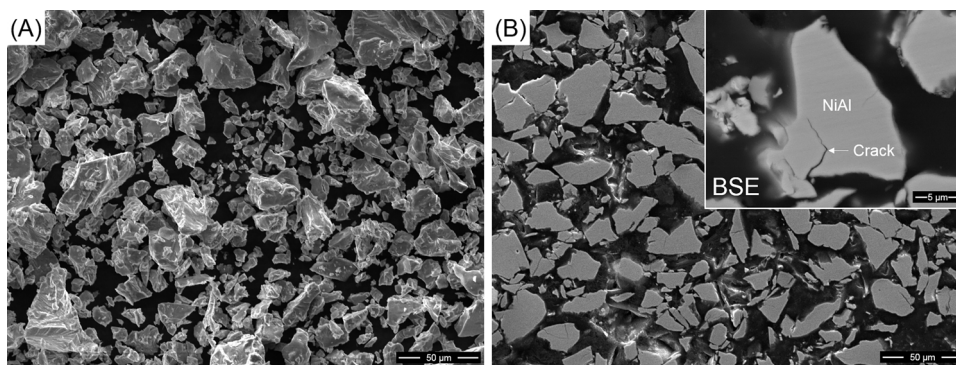


Fig. 2. SEM images of the (A) surface morphology and (B) cross-section of NiAl powder.

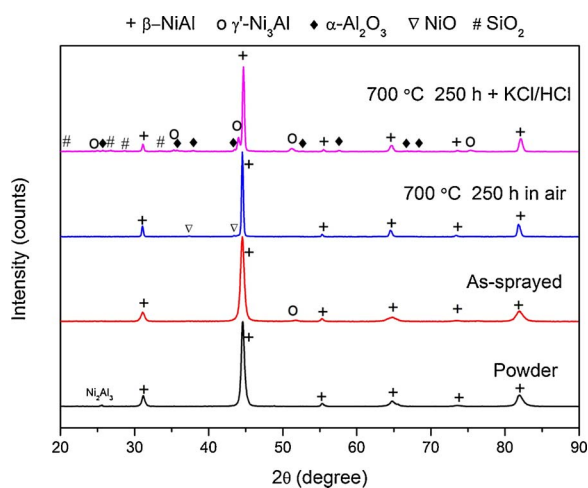


Fig. 3. XRD patterns of (from bottom to top) feedstock powder, as-sprayed coating, after oxidation at 700 °C for 250 h in air; and after corrosion at 700 °C for 250 h in synthetic gas with 500 ppm HCl and 10% KCl ash deposit (phase indexing: β -NiAl, γ' -Ni₃Al, α -Al₂O₃, NiO and SiO₂).

of the corrosion mechanism, which was always overlooked if only examined the area near the coating centre as described earlier in Fig. 4(C).

3.4. Corrosion of stainless steel substrate without NiAl coatings

The above results demonstrated that the stainless steel was well protected by the deposition of NiAl coating with the formation of stable Al₂O₃ throughout the coatings. As a contrast, Fig. 6(A) shows the microstructure and compositions of the corrosion products on a steel without NiAl coatings after the same corrosion test. Fig. 6(B) is the EDX map spectrum including identified elements superimposed on the characteristic X-ray peaks as well as the spectrum deconvolution of Mn and Cr peaks. Detailed composition of the corrosion products as examined by EDX point analysis is also listed in Table 3. Thick multi-layered and porous oxides are observed with a total thickness of 50–60 μ m, which already spalled from the steels surface. According to the EDX mappings, the outer layer (40–50 μ m) is composed of Fe-rich oxide; while the inner layer (10–15 μ m) is a mixture of Mn- and Cr-rich oxide; and Ni is observed throughout the entire oxide scale. In addition, in the middle of Fe-rich oxide layer, another thin Cr and Mn-rich oxide layer can also be observed. Beneath this thin layer, the oxide grains exhibit distinctive columnar morphology with a higher level of porosity in comparison with the oxide above this thin layer. More particularly, the columnar large grains are seen to be extended to the Cr-rich oxide layer while the top part is composed of Fe-rich oxide. A boundary can be seen in the middle of the columnar oxide grains with clear contrast under BSE mode in Fig. 6(A). On the other hand, after oxidation test without the presence of KCl/HCl, there is barely any oxide formed on

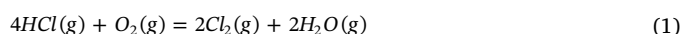
steels, not even a coherent layer. Fig. 6(B) shows a representative position where a spherical oxide is formed with a significantly small size in comparison with the oxide in Fig. 6(A). The EDX mappings show a similar oxide composition, which comprises an outer layer of Fe-rich oxide and inner layer of Cr-rich oxide. According to the XRD patterns in Fig. 7, the corrosion products are identified as mainly Fe₃O₄ and Fe₂O₃ with a minor fraction of Cr₂O₃ and FeCl₂. The oxidation products are mostly Fe₂O₃ and Fe₃O₄ phase; while the presence of Fe/Ni and Fe/Cr is due to partially spallation of oxides. It is obvious that during corrosion test, none of these oxide layer can effectively protect the stainless steels which eventually caused severe depletion of Fe, Cr and Mn in the alloy during corrosion test. It also indicates that the protection of NiAl coatings on steel against corrosion is effective with the formation of exclusive Al₂O₃. Nevertheless, the mechanism remains to be provided for the oxidation at the coating/substrate interface and the severe corrosion near the sample edges.

4. Discussion

In this section, thermodynamic analysis was carried out aiming at the predication of the phase and composition of the corrosion products at high temperatures using equilibrium phase diagrams in the alloy-O₂-Cl₂ systems. It is however worth noting that corrosion is essentially a non-equilibrium process with a degree of uncertainty of forming metastable phases [47]. In addition, the gas partial pressures as well as the composition of the alloy underneath are not constant, e.g. both Cr and Fe are depleted due to the fast growing oxide during corrosion, which significantly modify the alloy composition. Thus, large deviation of the calculated phase compositions from the experimental results is anticipated in materials that are far from the thermodynamic equilibrium. Nevertheless, it was suggested that the relevance and reliability of thermodynamic calculations can be improved significantly if their results are complemented by chemical and microstructural analyses [48]. In other words, the combination of the thermodynamic calculation with the experimental investigation of the phase composition in real samples extends the application potential of both methods.

4.1. Chlorine-induced corrosion of stainless steels at 700 °C

The high temperature corrosion of metallic materials by chlorine has been reported in numerous investigations on Fe-Cr alloys [23,49–52] and Ni-based alloys [53–55] in a similar chloridizing and oxidizing atmosphere with HCl (g) and O₂ (g). The main aggressive species in corrosion is however Cl₂ (g) (chlorine), not HCl (g), as reported by Abels et al. [30], at least for short exposure times. In a corrosion test, Cl₂ (g) partially comes from 500 ppm HCl (g) according to the following reaction in an atmosphere with 5% O₂ (g):



Although it is slow to reach equilibrium in gas phase, reaction (1) is

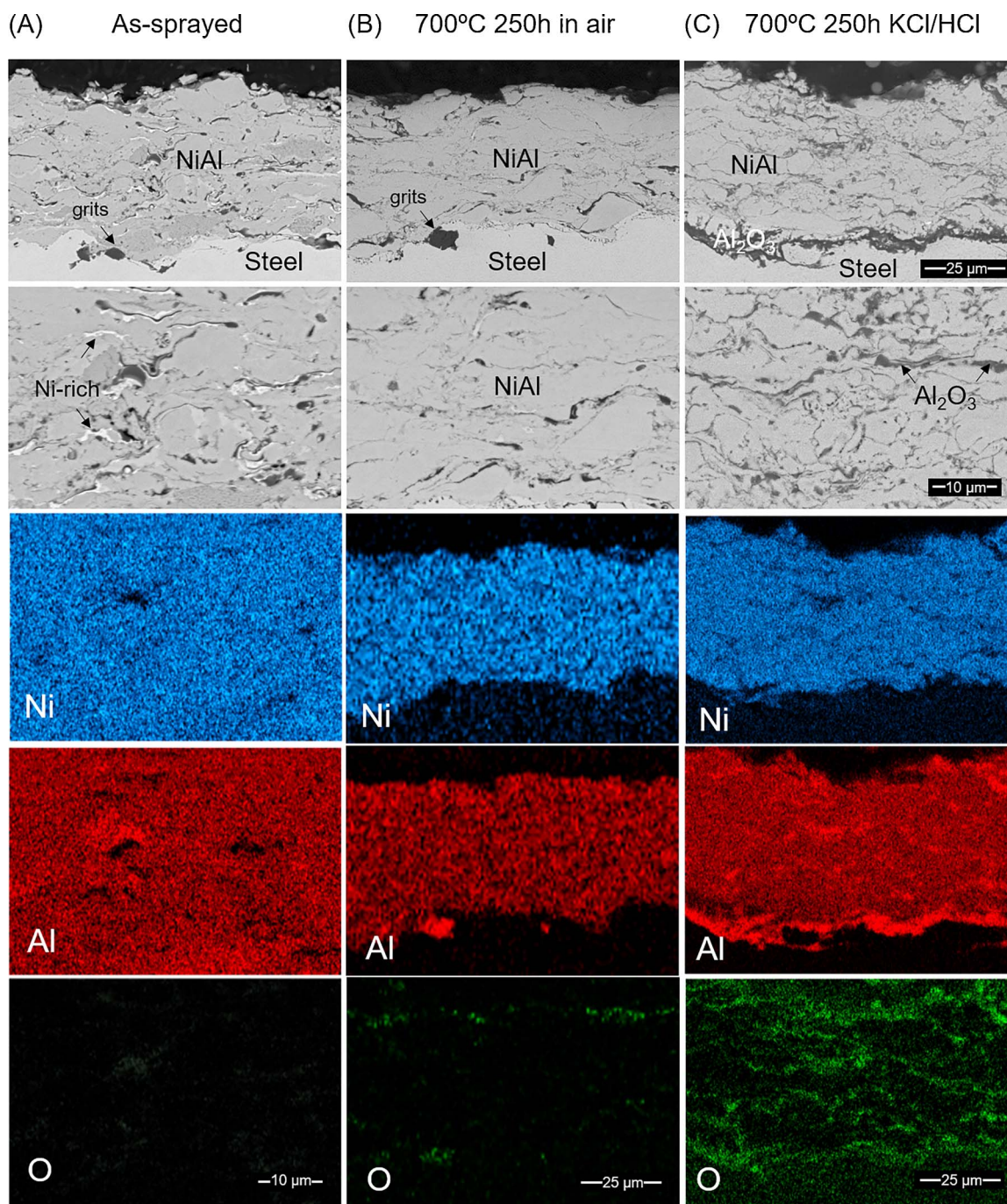


Fig. 4. Cross-sectional BSE images and EDX mappings of (A) as-sprayed NiAl coatings; (B) after oxidation at 700 °C for 250 h in air; and (C) after corrosion at 700 °C for 250 h in synthetic gas with 500 ppm HCl and 10% KCl ash deposit at low and high magnifications.

promoted by the consumption of Cl₂ at the metal surface, which makes the metal oxides act as catalysts for the reaction. The formation of Cl₂ could also be supplied by the 10% KCl salt in dry O₂ environment following:



It is well-established that the presence of Cl₂ in most cases prevents the formation of protective Cr₂O₃ layer and causes accelerated attack in

Table 2
Compositional analysis of the NiAl feedstock and coatings.

Element (wt.%)	Feedstock Powder		As-sprayed		After oxidation	After corrosion
	Supplier provided	EDX analysis	Ni-rich area	Other area		
Ni	69	68.3 ± 1.0	90.2 ± 3.6	66.7 ± 3.8	70.2 ± 0.3	71.2 ± 0.8
Al	31	31.7 ± 1.0	9.8 ± 3.6	33.3 ± 3.8	29.8 ± 0.3	28.8 ± 0.8

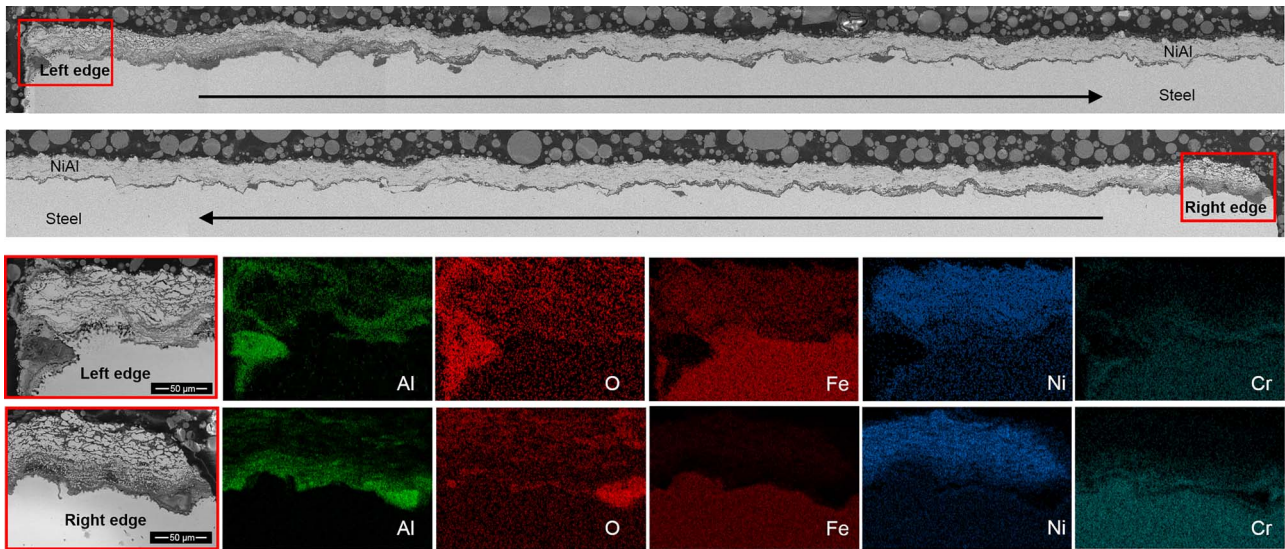


Fig. 5. Cross-sectional BSE images of NiAl coatings on the two edges after corrosion at 700 °C for 250 h in synthetic gas with 500 ppm HCl and 10% KCl ash deposit, and EDX mappings.

oxidizing environments [25]. In addition, according to studies on a number of Fe [56], Cr [57] and Ni [58] metal and alloys, there is always a strong correlation between corrosion mechanism and the Cl_2/O_2 ratio. This is because that the partial pressures of O_2 and Cl_2 determine the thermodynamic stability of metal chlorides and oxides at a given temperature. Thermodynamic phase stability diagrams for the metal-gas systems of Ni- O_2 - Cl_2 , Al- O_2 - Cl_2 , Fe- O_2 - Cl_2 and Cr- O_2 - Cl_2 at 700 °C are

shown in Fig. 8. The equilibrium condition for atmospheres containing 5% O_2 and 500 ppm HCl is marked on the diagrams which was first suggested by Zahr et al. [30]. It is worth mentioning that the actual Cl_2 partial pressure in this study should be higher than that due to the extra supply of Cl_2 from the 10% KCl deposit following reaction (2) but it is rather difficult to quantify the actual Cl_2 partial pressure values. Metal could either be oxidized or chloridized depending on the partial

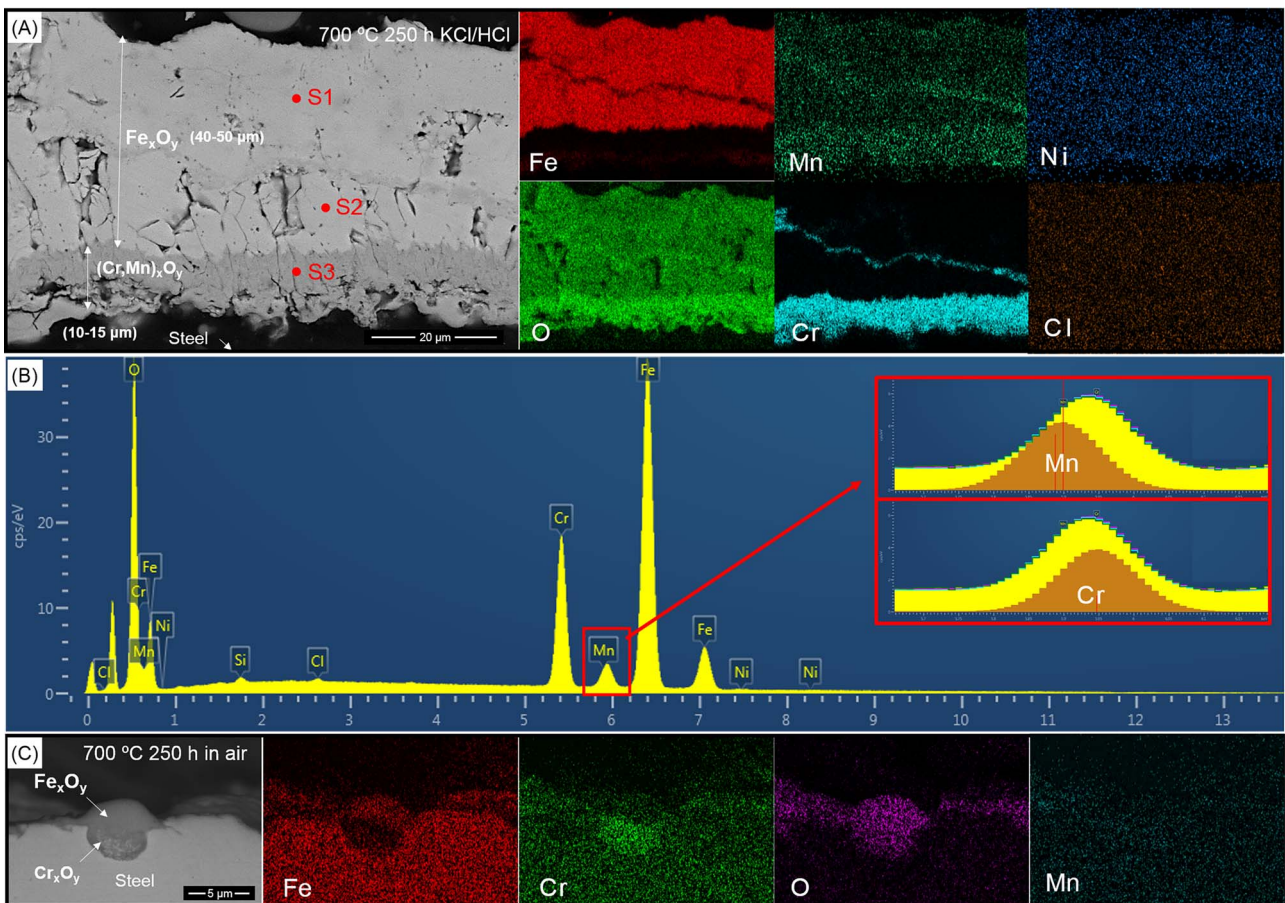


Fig. 6. BSE images and EDX mappings of (A) the thick multi-layered oxides on stainless steel without NiAl coatings after corrosion at 700 °C for 250 h in synthetic gas with 500 ppm HCl and 10% KCl ash deposit; (B) EDX map spectrum of the corrosion products with deconvolution of Mn and Cr peaks; and (C) thin oxide on steel after oxidation test at 700 °C for 250 h in air.

Table 3
Compositional analysis of oxide on the steel after corrosion.

Element (wt.%)	Map	S1	S2	S3
Fe	57.8	72.2	74.7	2.2
O	24.3	26.8	22.5	27.0
Cr	16.5	0.6	1.3	70.3
Mn	1.0	0.4	0.3	0.2
Ni	[†] 0.2	[†] 0.0	[†] 0.6	[†] 0.0
Cl	[†] 0.2	[†] 0.0	[†] 0.0	[†] 0.3

[†]Low confidence as indicated by the Aztec software.

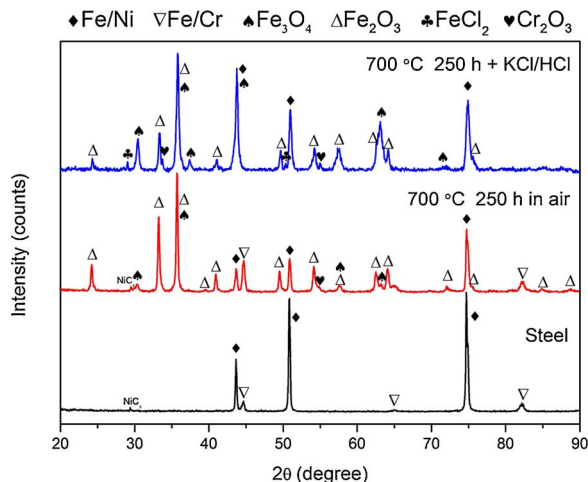
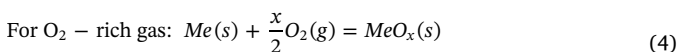
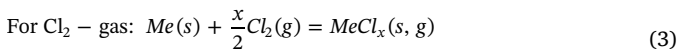


Fig. 7. XRD patterns of oxides on the steel before and after oxidation test and corrosion (top).

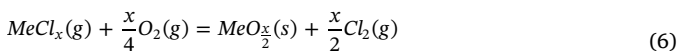
pressures of both O_2 and Cl_2 .



Chlorides are generally more volatile than oxides, and some of them are even in gaseous state (e.g. $AlCl_3$ (g)) at high temperatures. These solid chlorides also have considerable equilibrium vapor pressures and would evaporate continuously according to the following reaction:



The gaseous chlorides are more volatile and will also react with O_2 upon reaching regions with higher O_2 partial pressure to form oxides releasing gaseous Cl_2 according the following reaction:



This process is also known as “active oxidation” [58], which involves the formation of volatile metal chlorides and subsequent oxidation of the evaporating chlorides. As a result, Cl_2 acts as a catalyst, which significantly accelerates the growth of oxide on the metals. This could explain the fast growing oxide on the stainless steel after corrosion test as observed earlier in Fig. 6(A). Without Cl_2 , the oxidation reaction of stainless steel is much slower and the resulting oxide is negligible. The presence of Cl_2 have increased the oxide growth rate on steels over a magnitude of order higher as indicated by the huge difference in the thickness of oxides, which could be owing to the “active oxidation mechanism. The formation mechanism of thick multi-layered oxides on the steels, which contain a number of alloying elements, must have gone through even more complex corrosion mechanism, so the specific role of each element is difficult to differentiate.

The Corrosion of the FeCr(Ni) alloys has been extensively studied in different environments over a temperature range of 500–900 °C

[47,59–68]. It is generally known that the oxide scale typically consists of an outward growing Fe-rich layer and an inward growing layer consisting of spinel oxide; while the original metal/oxide interface separated the two layers. Thermo-Calc[®] software has also been used by Jonsson et al. [47,65] to interpret the formation mechanism of the oxide scale on FeCr(Ni) alloys. Fig. 9 shows the Thermo-Calc[®] calculation of oxide formation on 304 stainless steel (Fe-19Cr-9.3Ni-2Mn) as a dependency of O_2 partial pressures at 700 °C. With the decrease of pO_2 , a decrease of corundum content is seen along with an increase of spinel. This agrees well with the above description that the spinel layer formed underneath the corundum layer with the presence of lower pO_2 . As described earlier in Fig. 6(A), two distinctive types of oxide microstructures were observed being separated by a thin Cr-rich and Mn-rich layer, which is possibly the original metal/oxide interface. Kinetic factors also need to be considered that the observed elemental distributions in the scale were determined by the different diffusivities of cations [47,65]. The diagram of the cation diffusion co-efficient in spinel as a dependency of pO_2 at high temperatures shows that Cr^{3+} ions diffuse several orders of magnitude slower than Fe^{2+} and O^{2-} in the spinel [69,70], resulting in the formation of outward growing Fe-rich oxide and inward growing Cr-rich oxide, which agrees well with the experimental observations.

4.2. Oxidation of NiAl in air at 700 °C

According to the Ellingham diagram, Al_2O_3 is undoubtedly the most stable oxide among all the alloy oxides at high temperatures, which always forms last as the innermost oxide layer attached to the Al-containing alloys with the least amount of O_2 [71]. One of the key criteria for the formation of exclusive Al_2O_3 scale on the oxidation resistant alloys is the critical content of Al in the alloys being as a reservoir for the continuous growth of Al_2O_3 . In the Ni-Al binary alloy system, the critical value of Al% is about 16 wt.% (or ~30 at.%) for the formation of exclusive Al_2O_3 at temperatures of 900–1300 °C (See the oxide scale map for Ni-Al as a dependency of alloying compositions and temperatures [72]). Fig. 10 shows the Thermo-Calc[®] calculations of the oxide scale formation on a Ni-Al system as a dependency of Al content at 700 °C with the presence of 0.1 atm O_2 (same partial pressure was used for the oxidation tests in Ref. [72]). By increasing the Al content, the phase changes from γ -Ni to γ' -Ni₃Al and β -NiAl. As calculated, the critical content of Al in the Ni-Al alloys for the formation of exclusive Al_2O_3 is about 40 at.%, and lower content of Al (e.g. γ' -Ni₃Al) would result in the formation of a mixture of NiAl₂O₄ and NiO. More importantly, the growth of Al_2O_3 is a temperature-dependent process, and that is why the alumina-forming alloys are normally chosen at temperatures of over 900 °C for effective oxidation protection. According to the Arrhenius diagram of NiAl alloys [73], the parabolic rate constant k_p is extremely low, which is only about $10^{-15} \text{ g}^2/\text{cm}^4\text{s}$ with the formation of γ - Al_2O_3 , which is a transient oxide that will transform to stable α - Al_2O_3 if given sufficient time. This agrees with the observations in Fig. 4(B) that after oxidation at 700 °C for 250 h, there is barely any oxide on the NiAl coating surface or inside the coating. As a contrast in Fig. 4(C), with the presence of the KCl/HCl, severe oxidation occurred with the formation of more Al_2O_3 on the NiAl coating surface, inside the coating and at the coating-substrate interface. Among them, the k_p for the thick Al_2O_3 layer at the interface with a thickness of 3–5 μm can be estimated if assuming the alumina is fully dense. The estimated k_p is about $10^{-12} \text{ g}^2/\text{cm}^4\text{s}$, which is 3 orders of magnitude higher than the theoretic value at 700 °C. In addition, as shown in Fig. 5, more severe oxidation was observed near the sample edges with the formation of thicker Al_2O_3 layer alongside the coating/substrate interface with an even much higher k_p . All of these abnormal k_p suggest that the oxidation of NiAl coatings on steels with the presence of KCl/HCl did not follow the parabolic rate law for the growth of oxide scale on alloys surface.

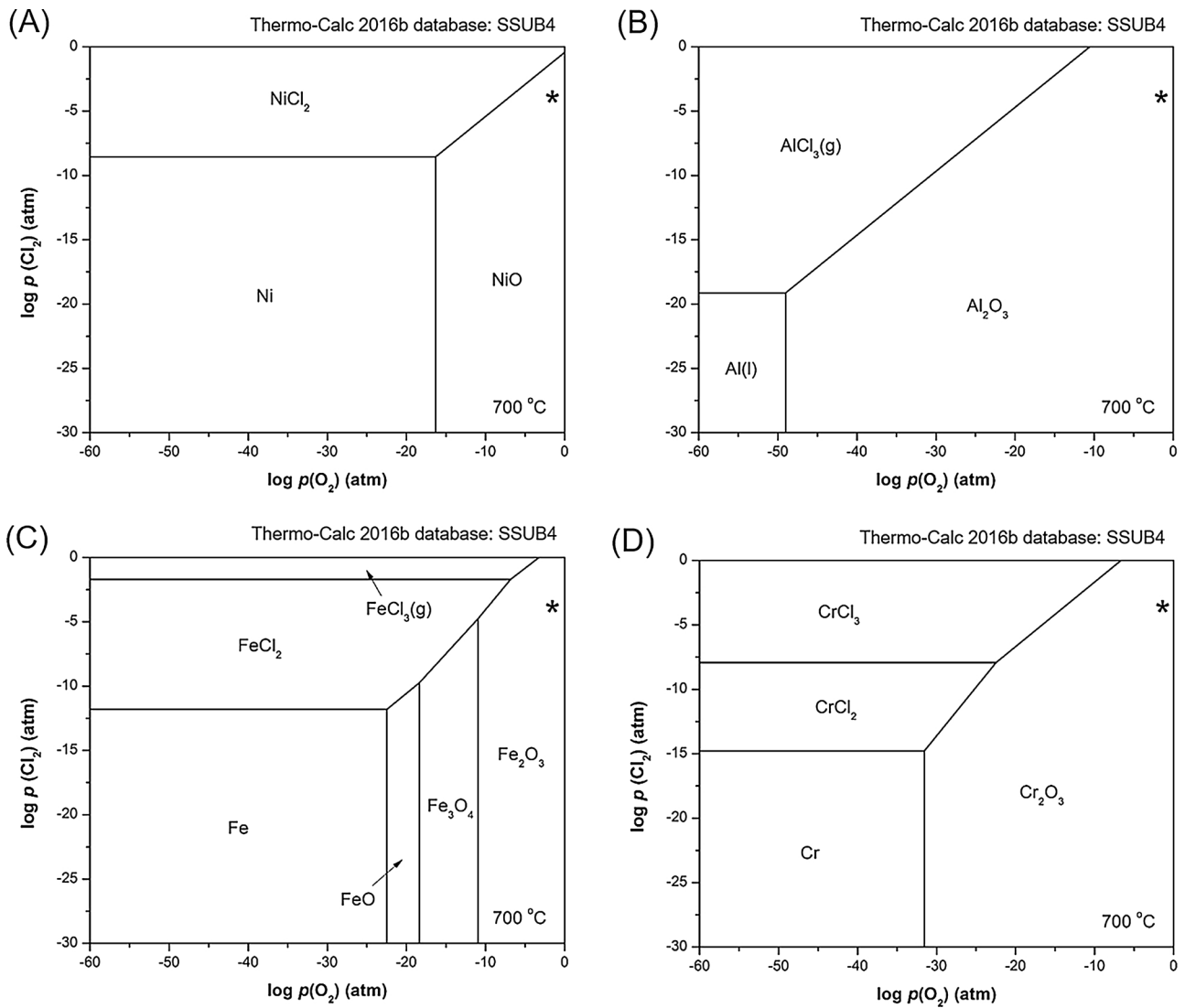


Fig. 8. Thermo-Calc[®] calculation of oxide formations on (A) Ni; (B) Al; (C) Fe; and (D) Cr at 700 °C as a dependency of O_2 and Cl_2 partial pressures. Thermo-Calc[®] (2016b) was used with SSUB4 databases.

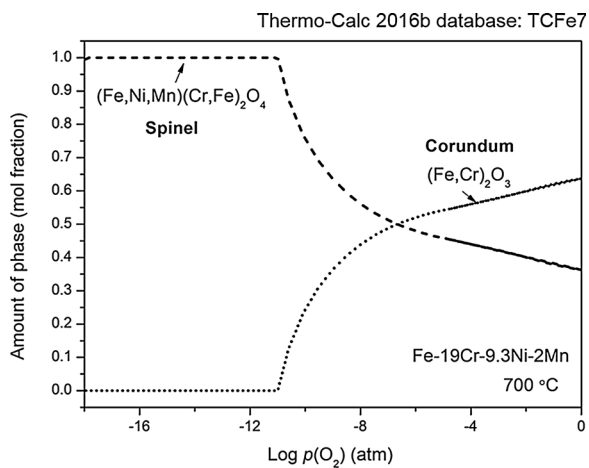


Fig. 9. Thermo-Calc[®] calculation of oxide formation on 304 stainless steel as a dependency of O_2 partial pressures at 700 °C. Thermo-Calc[®] (2016b) was used with TCFE7 database.

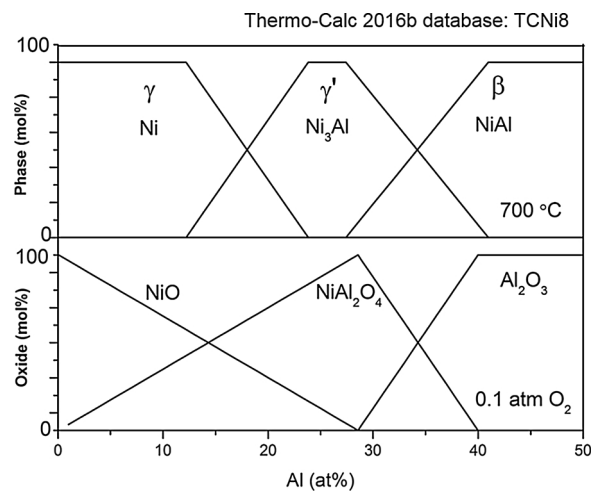


Fig. 10. Thermo-Calc[®] calculation of phase evolution (top) and oxide formations (bottom) on a Ni-Al alloy system at 700 °C as a dependency of Al content (from 0 to 50 at%) with a constant O_2 partial pressure of 0.1 atm. Thermo-Calc[®] (2016b) was used with TCNi8 and SSUB4 databases.

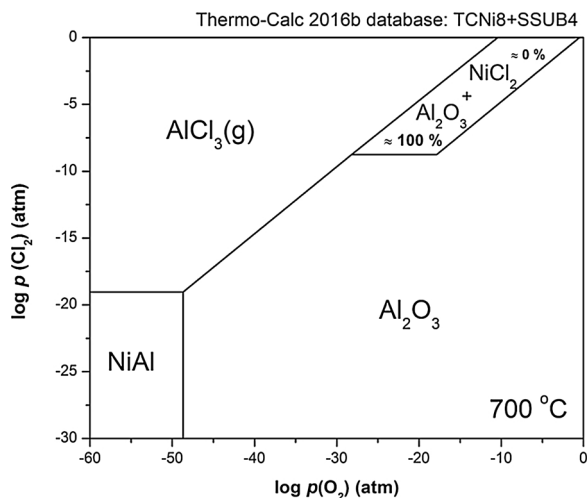
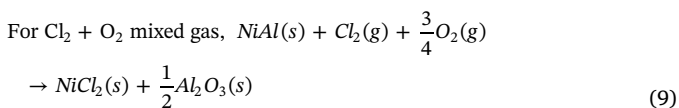
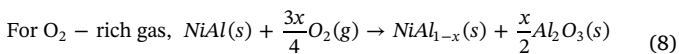
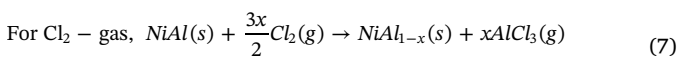


Fig. 11. Thermo-Calc[®] calculation of oxide formations on a NiAl alloy at 700 °C as a dependency of O₂ and Cl₂ partial pressures. Thermo-Calc[®] (2016b) was used with TCNi8 and SSUB4 databases.

4.3. Phase stability of NiAl-Cl₂-O₂ system at 700 °C

The real mechanism should follow the ‘active oxidation’ as mentioned earlier with Cl₂ acting as a catalyst, which significantly accelerates the growth of oxide. Fig. 11 shows the thermodynamic phase diagrams for the NiAl-O₂-Cl₂ system at 700 °C as calculated by Thermo-Calc[®] with a combined database of SSUB4 and TCNi8. Based on the phase diagram, depending on the partial pressure of O₂ and Cl₂, 3 possible reactions could occur on the NiAl alloys at 700 °C as follows,



For reaction (7), the gaseous AlCl₃ could further react with O₂ and form stable Al₂O₃ as follows,



Again, in combination of reactions (7) and (10), the Cl₂ (g) acts as a reaction catalyst in this “active oxidation” process and significantly accelerates the growth rate of Al₂O₃ in the NiAl coating. For reaction (9), it is calculated that the resulting products are composed of nearly 100 mol% of Al₂O₃ and only 1.39×10^{-16} mol% of NiCl₂ (s). Although, the formation of NiCl₂ (s) is scarce, this reaction could still be promoted due to the evaporation of NiCl₂ (g) as follows at the solid/gas interface.



The continuous evaporation of NiCl₂ (g) accelerates the rate of reaction (9) and results in the formation of more Al₂O₃. Accordingly, the formation of both volatile AlCl₃ (g) and NiCl₂ (g) in reaction (7) and (9), respectively, would contribute to the fast growing of Al₂O₃, especially at the coating/substrate interface where exists a gradient of vapor pressure from the sample centre to the edges. This explains why the corrosion near the sample edges was more severe than the sample centre as shown in Fig. 5. Furthermore, the depletion of Al due to the fast growing Al₂O₃ could result in a phase transformation to γ'-Ni₃Al and form more volatile and non-protective oxide, such as NiO and NiAl₂O₄ (spinel). Fig. 12 shows the thermodynamic phase stability diagrams for the Ni₃Al-O₂-Cl₂ system at 700 °C as calculated by

Thermo-Calc[®] with a combined database of SSUB4 and TCNi8. For γ'-Ni₃Al, more volatile oxides and chlorides could form with the presence of Cl₂ and O₂, such as NiCl₂, NiO and NiAl₂O₄. All of them are fast growing products, but none is as protective as Al₂O₃ and therefore should be avoided. Once a coherent Al₂O₃ scale forms on the alloy surface, it inhibits the formation of other volatile oxides and therefore protects the alloy.

4.4. Protectiveness of NiAl coatings against corrosion

In summary, the initial objective of this study was to investigate the protectiveness of the Al₂O₃-forming NiAl coating in a KCl/HCl containing environment. It was surprising that the Al₂O₃ scale mainly formed at the coating/substrate interface but not on the coating surface, with an unexpected higher growth rate than the theoretical value at this low temperature. In order to explain the mechanism for the fast growing Al₂O₃, the cross-section of the entire coating was carefully examined using SEM/EDX including both sample edges. It was found that corrosion started from the sample edges and propagated through the coating/substrate interface towards the inner sections of the specimen. Although ideally this issue could be avoided if the steel was fully coated with NiAl, it is indeed difficult to guarantee that no defects or cracks could still exist in the coatings that could initiate the corrosion. In addition, chlorine is well known for its rapid penetration through scale that the chlorine itself (or Cl⁻ ion) pushes its way through the oxide by cracking, grain boundary grooving or fissuring through scale and alloys [51]. It therefore makes such specific mechanism at the sample edges more useful to explain similar chlorine induced corrosion problems in many industrial cases. On the other hand, it is reasonable to believe that the superior inertness of the NiAl coatings also contributed to the protection of steel against corrosion. However, chlorine could still penetrate the NiAl coating itself possibly through defects (e.g. pores, cracks, etc.) or grain boundaries. This was supported by the observation of a higher content of Al₂O₃ inside the NiAl coatings than the oxidized sample in air. Nevertheless, it is clear that the chlorine was not able to further penetrate the Al₂O₃ scale at the coating/substrate interface, which ultimately protected the steel underneath from corrosion attack. The durability of this multi-layered system, i.e. the adhesion between each two layers, however remains to be examined, that could be adversely affected by the large thermal expansion mismatch upon thermal cycling. Nevertheless, more in-depth experimental investigations are required to validate the corrosion mechanism as proposed in this study (e.g. more interrupted tests with shorter durations). Direct observation of the formation of any chloride after corrosion could be challenging due to the volatile nature of gaseous AlCl₃ and the trace amount of NiCl₂, which might not be detectable.

5. Conclusions

In this study, β-NiAl coatings were deposited by HVOF thermal spray onto stainless steels for protection against chlorine-induced corrosion in biomass-fueled boilers. The steels were well protected after a corrosion test at 700 °C for 250 h in an environment of a synthetic flue gas of 5% O₂, 500 ppm HCl and balance N₂, and deposit salt containing 10% KCl. Severe corrosion was observed with the fast growing Al₂O₃ at the NiAl- steel interface starting from the sample edges to the centre where both Cl₂ and O₂ diffuse into and corrode the samples. From Thermo-Calc[®] calculations, the corrosion mechanism is suggested to follow the “active oxidation” process, in which Cl₂ acts as a catalyst. It involves the formation of volatile gaseous NiCl₂ and AlCl₃ and subsequent oxidation and evaporation as driven by the gradient of the vapor pressure along the coating-substrate interface, which significantly promotes the growth of Al₂O₃. This study has demonstrated that although NiAl coatings are effective in corrosion protection of steels, it is essential to avoid any direct exposure of coating/steel interface to the Cl₂/O₂ gases, which could significantly deplete the Al and transform to γ'-Ni₃Al after long-term service.

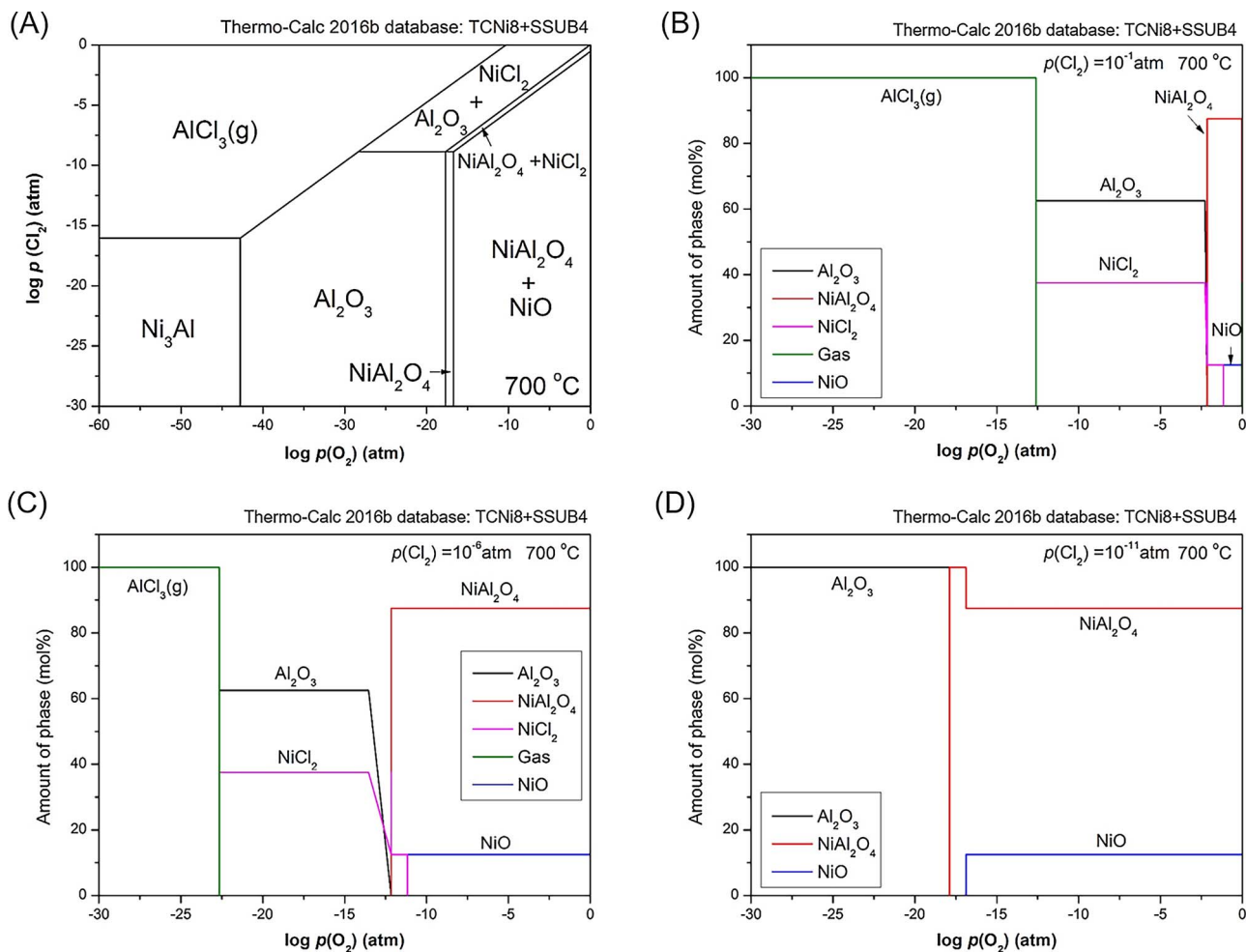


Fig. 12. Thermo-Calc[®] calculation of oxide formations on a Ni₃Al alloy at 700 °C (A) as a dependency of O₂ and Cl₂ partial pressures; and with a constant Cl₂ partial pressure of (B) 10⁻¹ atm; (C) 10⁻⁶ atm; and (D) 10⁻¹¹ atm. Thermo-Calc[®] (2016b) was used with TCNi8 and SSUB4 databases.

Acknowledgements

This work was supported by the Engineering and Physical Sciences Research Council [grant number EP/M01536X/1]. The authors would like to acknowledge Prof. Graham McCartney from the University of Nottingham and Mr. Esmail Sadeghimeresht from the University West for access to the thermo-dynamic software, and Mr. Rory Screamor for the experimental assistance in thermal spray. Dr. Mingwen Bai acknowledges many helpful discussions on power plant materials with Prof. Hao Liu and Prof. Wei Sun at the University of Nottingham during the USC-CFB-CMM project meetings. Special thanks to Prof. Bruce A. Pint for the helpful suggestions on our experiments.

References

- [1] A.A. Khan, W. de Jong, P.J. Jansens, H. Spliethoff, Biomass combustion in fluidized bed boilers: potential problems and remedies, *Fuel Process. Technol.* 90 (2009) 21–50.
- [2] A. Demirbas, Potential applications of renewable energy sources, biomass combustion problems in boiler power systems and combustion related environmental issues, *Prog. Energy Combust. Sci.* 31 (2005) 171–192.
- [3] M. Oksa, T. Varis, K. Ruusuvaari, Performance testing of iron based thermally sprayed HVOF coatings in a biomass-fired fluidised bed boiler, *Surf. Coat. Technol.* 251 (2014) 191–200.
- [4] W.H. Yeo, A.T. Fry, J. Purbolaksono, S. Ramesh, J.I. Inayat-Hussain, H.L. Liew, et al., Oxide scale growth and presumed exfoliation in a 700 °C or higher steam condition: a simulation study for future operations of ultra-supercritical power plants, *J. Supercrit. Fluids* 92 (2014) 215–222.
- [5] Y. Fukuda, Development of advanced ultra supercritical fossil power plants in Japan: materials and high temperature corrosion properties, *Mater. Sci. Forum: Trans. Tech. Publ.* (2011) 236–241.
- [6] N. Bala, H. Singh, S. Prakash, J. Karthikeyan, Investigations on the behavior of HVOF and cold sprayed Ni-20Cr coating on T22 boiler steel in actual boiler environment, *J. Therm. Spray Technol.* 21 (2012) 144–158.
- [7] S. Paul, M.D.F. Harvey, Corrosion testing of Ni alloy HVOF coatings in high temperature environments for biomass applications, *J. Therm. Spray Technol.* 22 (2013) 316–327.
- [8] S. Hong, Y. Wu, G. Li, B. Wang, W. Gao, G. Ying, Microstructural characteristics of high-velocity oxygen-fuel (HVOF) sprayed nickel-based alloy coating, *J. Alloys Compd.* 581 (2013) 398–403.
- [9] H. Al-Fadhli, J. Stokes, M. Hashmi, B. Yilbas, The erosion–corrosion behaviour of high velocity oxy-fuel (HVOF) thermally sprayed inconel-625 coatings on different metallic surfaces, *Surf. Coat. Technol.* 200 (2006) 5782–5788.
- [10] S. Bluni, A. Marder, Effects of thermal spray coating composition and microstructure on coating response and substrate protection at high temperatures, *Corrosion* 52 (1996) 213–218.
- [11] H. Edris, D. McCartney, A. Sturgeon, Microstructural characterization of high velocity oxy-fuel sprayed coatings of Inconel 625, *J. Mater. Sci.* 32 (1997) 863–872.
- [12] T. Hussain, T. Dudziak, N. Simms, J. Nicholls, Fireside corrosion behavior of HVOF and plasma-sprayed coatings in advanced coal/biomass co-fired power plants, *J. Therm. Spray Technol.* 22 (2013) 797–807.
- [13] M. Oksa, P. Auerkari, J. Salonen, T. Varis, Nickel-based HVOF coatings promoting high temperature corrosion resistance of biomass-fired power plant boilers, *Fuel Process. Technol.* 125 (2014) 236–245.
- [14] M. Uusitalo, P. Vuoristo, T. Mäntylä, High temperature corrosion of coatings and boiler steels in reducing chlorine-containing atmosphere, *Surf. Coat. Technol.* 161 (2002) 275–285.
- [15] H.P. Michelsen, F. Frandsen, K. Dam-Johansen, O.H. Larsen, Deposition and high temperature corrosion in a 10 MW straw fired boiler, *Fuel Process. Technol.* 54 (1998) 95–108.
- [16] M. Montgomery, A. Karlsson, In-situ corrosion investigation at Masnedø CHP plant? a straw-fired power plant, *Mater. Corros.* 50 (1999) 579–584.
- [17] H.P. Nielsen, F.J. Frandsen, K. Dam-Johansen, Lab-scale investigations of high-temperature corrosion phenomena in straw-fired boilers, *Energy Fuels* 13 (1999) 1114–1121.
- [18] Y. Shu, F. Wang, W. Wu, Synergistic effect of NaCl and water vapor on the corrosion

- of 1Cr-11Ni-2W-2Mo-V steel at 500–700°C, *Oxid. Metals* 51 (1999) 97–110.
- [19] C. Pettersson, J. Pettersson, H. Asteman, J.E. Svensson, L.G. Johansson, KCl-induced high temperature corrosion of the austenitic Fe–Cr–Ni alloys 304L and Sanicro 28 at 600°C, *Corros. Sci.* 48 (2006) 1368–1378.
- [20] J. Pettersson, N. Folkesson, L.-G. Johansson, J.-E. Svensson, The effects of KCl, K₂SO₄ and K₂CO₃ on the high temperature corrosion of a 304-type austenitic stainless steel, *Oxid. Metals* 76 (2011) 93–109.
- [21] H. Asteman, M. Spiegel, A comparison of the oxidation behaviours of Al₂O₃ formers and Cr₂O₃ formers at 700°C-oxide solid solutions acting as a template for nucleation, *Corros. Sci.* 50 (2008) 1734–1743.
- [22] H. Josefsson, F. Liu, J.E. Svensson, M. Halvarsson, L.G. Johansson, Oxidation of FeCrAl alloys at 500–900°C in dry O₂, *Mater. Corros.* 56 (2005) 801–805.
- [23] Y.S. Li, Y. Niu, M. Spiegel, High temperature interaction of Al/Si-modified Fe-Cr alloys with KCl, *Corros. Sci.* 49 (2007) 1799–1815.
- [24] N. Israelsson, J. Engkvist, K. Hellström, M. Halvarsson, J.-E. Svensson, L.-G. Johansson, KCl-induced corrosion of an FeCrAl alloy at 600°C in O₂ + H₂O environment: the effect of pre-oxidation, *Oxid. Metals* 83 (2015) 29–53.
- [25] N. Israelsson, K.A. Unocic, K. Hellstrom, T. Jonsson, M. Norell, J.E. Svensson, et al., A microstructural and kinetic investigation of the KCl-induced corrosion of an FeCrAl alloy at 600°C, *Oxid. Metals* 84 (2015) 105–127.
- [26] Y. Li, M. Spiegel, S. Shimada, Corrosion behaviour of various model alloys with NaCl/KCl coating, *Mater. Chem. Phys.* 93 (2005) 217–223.
- [27] J. Nicholls, Advances in coating design for high-performance gas turbines, *MRS Bull.* 28 (2003) 659–670.
- [28] Z. Pala, M. Bai, F. Lukac, T. Hussain, Laser clad and HVOF-sprayed stellite 6 coating in chlorine-rich environment with KCl at 700°C, *Oxid. Metals* 88 (2017) 749–771.
- [29] L. Reddy, P. Shipway, C. Davis, T. Hussain, HVOF and laser-clad Fe–Cr–B coating in simulated biomass combustion: microstructure and fireside corrosion, *Oxid. Metals* 87 (2017) 825–835.
- [30] A. Zahs, M. Spiegel, H.J. Grabke, Chloridation and oxidation of iron, chromium, nickel and their alloys in chloridizing and oxidizing atmospheres at 400–700°C, *Corros. Sci.* 42 (2000) 1093–1122.
- [31] A. Kroupa, Modelling of phase diagrams and thermodynamic properties using Calphad method – development of thermodynamic databases, *Comput. Mater. Sci.* 66 (2013) 3–13.
- [32] N. Saunders, A.P. Miodownik, CALPHAD (calculation of Phase Diagrams): a Comprehensive Guide, Elsevier, 1998.
- [33] H.L. Lukas, S.G. Fries, B. Sundman, *Computational Thermodynamics: the Calphad Method*, Cambridge University Press, Cambridge, 2007.
- [34] J.O. Andersson, T. Helander, L. Höglund, P. Shi, B. Sundman, Thermo-Calc & DICTRA, computational tools for materials science, *Calphad* 26 (2002) 273–312.
- [35] J. Bratberg, H. Mao, L. Kjellqvist, A. Engström, P. Mason, Q. Chen, The development and validation of a new thermodynamic database for Ni-based alloys, *Superalloys* 12 (2012) 803–812.
- [36] B. Gorr, H.-J. Christ, D. Mukherji, J. Röslér, Thermodynamic calculations in the development of high-temperature Co–Re-based alloys, *J. Alloys Compd.* 582 (2014) 50–58.
- [37] O. Bergman, Influence of oxygen partial pressure in sintering atmosphere on properties of Cr–Mo prealloyed powder metallurgy steel, *Powder Metall.* 50 (2007) 243–249.
- [38] T.J. Nijdam, W.G. Sloof, Microstructural evolution of a MCrAlY coating upon isothermal annealing, *Mater. Charact.* 59 (2008) 1697–1704.
- [39] K. Ma, J.M. Schoenung, Thermodynamic investigation into the equilibrium phases in the NiCoCrAl system at elevated temperatures, *Surf. Coat. Technol.* 205 (2010) 2273–2280.
- [40] K. Ma, F. Tang, J.M. Schoenung, Investigation into the effects of Fe additions on the equilibrium phase compositions, phase fractions and phase stabilities in the Ni–Cr–Al system, *Acta Mater.* 58 (2010) 1518–1529.
- [41] J. Liang, H. Wei, Y. Zhu, T. Jin, X. Sun, Z. Hu, Phase stabilities in a NiCrAlYRe coating alloy, *Surf. Coat. Technol.* 206 (2012) 2746–2750.
- [42] J. Liang, H. Wei, Y. Zhu, X. Sun, Z. Hu, M. Dargusch, et al., Phase constituents and thermal expansion behavior of a NiCrAlYRe coating alloy, *J. Mater. Sci.* 46 (2011) 500–508.
- [43] B. Baufeld, M. Schmücker, Microstructural evolution of a NiCoCrAlY coating on an IN100 substrate, *Surf. Coat. Technol.* 199 (2005) 49–56.
- [44] D.R.G. Achar, R. Munoz-Arroyo, L. Singheiser, W.J. Quadackers, Modelling of phase equilibria in MCrAlY coating systems, *Surf. Coat. Technol.* 187 (2004) 272–283.
- [45] L.T. Wu, R.T. Wu, P. Xiao, T. Osada, K.I. Lee, M. Bai, A prominent driving force for the spallation of thermal barrier coatings: chemistry dependent phase transformation of the bond coat, *Acta Mater.* 137 (2017) 22–35.
- [46] A. Roine, HSC Chemistry, Outokumpu Research Oy, Pori, Finland, 2002.
- [47] T. Jonsson, H. Larsson, S. Karlsson, H. Hooshyar, M. Sattari, J. Liske, et al., High-temperature oxidation of FeCr (Ni) alloys: the behaviour after Breakaway, *Oxid. Metals* 87 (2017) 333–341.
- [48] M. Born, J. Korb, D. Rafaja, M. Dopita, R.W. Schüle, Capability of thermodynamic calculation in the development of alloys for deposition of corrosion-protection coatings via thermal spraying, *Mater. Corros.* 58 (2007) 673–680.
- [49] X. Zheng, R.A. Rapp, Chloridation-oxidation of nine commercial high-temperature alloys at 800°C, *Oxid. Metals* 48 (1997) 553–596.
- [50] A. Kim, M. McNallan, Mixed Oxidation of Iron–Chromium Alloys in Gases Containing Oxygen and Chlorine at 900–1200°K, *Corrosion* 46 (1990) 746–755.
- [51] H.J. Grabke, E. Reese, M. Spiegel, The effects of chlorides, hydrogen-chloride, and sulfur-dioxide in the oxidation of steels below deposits, *Corros. Sci.* 37 (1995) 1023–1043.
- [52] M. Spiegel, C. Schroer, H.J. Grabke, Corrosion of high alloy steels and Fe-Cr-alloys beneath deposits from waste incinerator plants, *Mater. Sci. Forum: Trans. Tech. Publ.* (1997) 527–534.
- [53] J.-M. Abels, H.-H. Strehblow, A surface analytical approach to the high temperature chlorination behaviour of inconel 600 at 700°C, *Corros. Sci.* 39 (1997) 115–132.
- [54] H. Chu, P. Datta, K. Strafford, Corrosion behavior of Fe (Ni) CrAlX alloys in an HCl-H₂O-H₂ gas mixture at 800°C, *Oxid. Metals* 43 (1995) 491–508.
- [55] R. Prescott, F. Stott, P. Elliott, Investigations of the degradation of high-temperature alloys in a potentially oxidizing-chloridizing gas mixture, *Oxid. Metals* 31 (1989) 145–166.
- [56] K. Strafford, P. Datta, G. Forster, High-temperature chloridation of binary Fe Cr alloys at 1000°C, *Mater. Sci. Eng. A* 120 (1989) 61–68.
- [57] Y. Shinata, M. Hara, T. Nakagawa, Accelerated oxidation of chromium by trace of sodium chloride vapor, *Mater. Trans. JIM* 32 (1991) 969–972.
- [58] Y. Lee, M. McNallan, Ignition of nickel in environments containing oxygen and chlorine, *Metall. Mater. Trans. A* 18 (1987) 1099–1107.
- [59] T. Jonsson, F. Liu, S. Canovic, H. Asteman, J.-E. Svensson, L.-G. Johansson, et al., Influence of H₂O (g) on the oxide microstructure of the stainless steel 353MA at 900°C in oxygen, *J. Electrochem. Soc.* 154 (2007) C603–C610.
- [60] T. Jonsson, J. Froitzheim, J. Pettersson, J.-E. Svensson, L.-G. Johansson, M. Halvarsson, The influence of KCl on the corrosion of an austenitic stainless steel (304L) in oxidizing humid conditions at 600°C: a microstructural study, *Oxid. Metals* 72 (2009) 213–239.
- [61] T. Jonsson, N. Folkesson, J.-E. Svensson, L.-G. Johansson, M. Halvarsson, An ESEM in situ investigation of initial stages of the KCl induced high temperature corrosion of a Fe–2.25 Cr–1Mo steel at 400°C, *Corros. Sci.* 53 (2011) 2233–2246.
- [62] B. Pujilaksono, T. Jonsson, H. Heidari, M. Halvarsson, J.-E. Svensson, L.-G. Johansson, Oxidation of binary FeCr alloys (Fe–2.25 Cr, Fe–10Cr, Fe–18Cr and Fe–25Cr) in O₂ and in O₂ + H₂O environment at 600°C, *Oxid. Metals* 75 (2011) 183–207.
- [63] T. Jonsson, B. Pujilaksono, H. Heidari, F. Liu, J.-E. Svensson, M. Halvarsson, et al., Oxidation of Fe–10Cr in O₂ and in O₂ + H₂O environment at 600°C: a microstructural investigation, *Corros. Sci.* 75 (2013) 326–336.
- [64] T. Jonsson, N. Folkesson, M. Halvarsson, J.-E. Svensson, L.-G. Johansson, Microstructural investigation of the HCl-induced corrosion of the austenitic alloy 310S (52Fe26Cr19Ni) at 500°C, *Oxid. Metals* 81 (2014) 575–596.
- [65] T. Jonsson, S. Karlsson, H. Hooshyar, M. Sattari, J. Liske, J.-E. Svensson, et al., Oxidation after breakdown of the chromium-rich scale on stainless steels at high temperature: internal oxidation, *Oxid. Metals* 85 (2016) 509–536.
- [66] M. Halvarsson, J.E. Tang, H. Asteman, J.-E. Svensson, L.-G. Johansson, Microstructural investigation of the breakdown of the protective oxide scale on a 304 steel in the presence of oxygen and water vapour at 600°C, *Corros. Sci.* 48 (2006) 2014–2035.
- [67] G.H. Meier, K. Jung, N. Mu, N.M. Yanar, F.S. Pettit, J. Pirón Abellán, et al., Effect of alloy composition and exposure conditions on the selective oxidation behavior of ferritic Fe–Cr and Fe–Cr–X alloys, *Oxid. Metals* 74 (2010) 319–340.
- [68] H. Hooshyar, T. Jonsson, J. Hall, J.-E. Svensson, L. Johansson, J. Liske, The effect of H₂ and H₂O on the oxidation of 304L-stainless steel at 600°C: general behaviour (part I), *Oxid. Metals* 85 (2016) 321–342.
- [69] J.A. Van Orman, K.L. Crispin, Diffusion in oxides, *Rev. Mineral. Geochem.* 72 (2010) 757–825.
- [70] J. Töpfer, S. Aggarwal, R. Dieckmann, Point defects and cation tracer diffusion in (Cr_xFe_{1-x})₃₋₈O₄ spinels, *Solid State Ionics* 81 (1995) 251–266.
- [71] J.A. Nychka, D.R. Clarke, G.H. Meier, Spallation and transient oxide growth on PWA 1484 superalloy, *Mater. Sci. Eng. A* 490 (2008) 359–368.
- [72] B. Gleeson, N. Mu, S. Hayashi, Compositional factors affecting the establishment and maintenance of Al₂O₃ scales on Ni–Al–Pt systems, *J. Mater. Sci.* 44 (2009) 1704–1710.
- [73] H. Grabke, Oxidation of NiAl and FeAl, *Intermetallics* 7 (1999) 1153–1158.